

**EUROPEAN COMMISSION**

HORIZON 2020 PROGRAMME  
TOPIC H2020-LCE-07-2016-2017

Developing the next generation technologies of renewable electricity and  
heating/cooling

GA No. 727523

**Next – generation interdigitated back-contacted silicon  
heterojunction solar cells and modules by design and  
process innovations**



**NextBase - Deliverable report**

**D8.3 – Report on the rear design of high efficiency IBC-SHJ  
solar cells**

<b>Deliverable No.</b>	NextBase D8.3	
<b>Related WP</b>	WP8	
<b>Deliverable Title</b>	Report on the rear design of high efficiency IBC-SHJ solar cells	
<b>Deliverable Date</b>		
<b>Deliverable Type</b>	Report	
<b>Dissemination level</b>	Confidential – member only (CO)	
<b>Author(s)</b>	Johann-Christoph Stang	15-09-2018
<b>Checked by</b>	Antonin Fejfar	20-09-2018
<b>Reviewed by (if applicable)</b>	Eb members	25-09-2018
<b>Approved by</b>	Kaining Ding (Coordinator)	28-09-2018
<b>Status</b>	Final	

### *Disclaimer/ Acknowledgment*



Copyright ©, all rights reserved. This document or any part thereof may not be made public or disclosed, copied or otherwise reproduced or used in any form or by any means, without prior permission in writing from the NextBase Consortium. Neither the NextBase Consortium nor any of its members, their officers, employees or agents shall be liable or responsible, in negligence or otherwise, for any loss, damage or expense whatever sustained by any person as a result of the use, in any manner or form, of any knowledge, information or data contained in this document, or due to any inaccuracy, omission or error therein contained.

All Intellectual Property Rights, know-how and information provided by and/or arising from this document, such as designs, documentation, as well as preparatory material in that regard, is and shall remain the exclusive property of the NextBase Consortium and any of its members or its licensors. Nothing contained in this document shall give, or shall be construed as giving, any right, title, ownership, interest, license or any other right in or to any IP, know-how and information.

This project has received funding from the European Union’s Horizon 2020 research and innovation programme under grant agreement No 727523. The information and views set out in this publication does not necessarily reflect the official opinion of the European Commission. Neither the European Union institutions and bodies nor any person acting on their behalf, may be held responsible for the use which may be made of the information contained therein.

## Publishable summary

We have used analytical calculations and numerical simulations to optimise the contact geometry of IBC-SHJ solar cells. Using the analytical calculations presented in the beginning, it becomes clear, more effort should be put into decreasing the contact resistivities, especially the one of the p-contact, which usually exhibits much higher values than its n-contact counterpart.

Key to optimising the contact layer stack and thus reducing the contact resistivity is using doped layers with low activation energies, or TCO materials with an appropriate work function. For the n-contact, doped layers with low activation energies will work with any TCO material; for n-contact layers with higher activation energies, the TCO's work function should be as low as possible.

For the p-contact, a wide band gap material as an incubation layer in combination with a p-type layer with a low activation energy yields low contact resistivities even for TCO materials with a lower work function. In case of a p-contact layer with a higher activation energy, TCO materials with higher work functions are necessary to enable efficient current extraction.

## Contents

1	Introduction.....	6
2	Reducing Resistive Losses by Optimising the Contact Geometry (HZB) .....	7
2.1	Geometrical Implications of the Contact Resistivities .....	7
2.2	Validation with Sentaurus .....	9
2.3	Metallisation Gaps and Overlap .....	9
2.4	Conclusion .....	11
3	Optimisation of the Contact Layer Stack (TUD) .....	12
3.1	Contact Selectivity & Selective Transport .....	12
3.2	Activation energy of doped layers .....	13
3.3	TCO work-function .....	14
3.4	Band gap of p-type contact .....	15
3.5	Summary .....	16
4	Conclusion and next steps.....	18
5	References.....	19

## List of acronyms, abbreviations and definitions

Table 1.1 Acronym table

Abbreviation	Explanation
<b>a-Si:H</b>	Hydrogenated amorphous silicon
<b>c-Si</b>	Crystalline silicon
<b>E<sub>a</sub></b>	Activation energy
<b>E<sub>g</sub></b>	Band gap
<b>FF</b>	Fill factor
<b>IBC</b>	Interdigitated back contact
<b>nc-Si:H</b>	Hydrogenated nanocrystalline silicon
<b>Φ<sub>cSi</sub></b>	c-Si band bending
<b>r<sub>TCO</sub></b>	TCO thickness
<b>SHJ</b>	Silicon heterojunction
<b>TCO</b>	Transparent conductive oxide
<b>V<sub>bi</sub></b>	Built-in voltage
<b>V<sub>oc</sub></b>	Open-circuit voltage
<b>WF<sub>TCO</sub></b>	TCO work function

# 1 Introduction

The rear side of an IBC SHJ solar cell contains both the electron and the hole selective contact of the solar cell, and thus accounts for loss mechanisms related to current transport (resistive losses) and recombination, with the former being predominant in silicon heterojunction solar cells. The *rear design* of an IBC SHJ solar cell therefore has to be thoroughly optimised in order to achieve efficiency values in the desired range of 26 % and above.

The rear design of the IBC SHJ solar cell refers to the contact geometry, describing the division of the total rear side area into the electron (n or BSF) and the hole (p or emitter) contact region as well as the magnitude of the metallisation gap. The contact geometry therefore relates to the horizontal dimension of the rear design. In contrast, the rear layer stack represents the vertical dimension of the rear design, as it determines the current transport capabilities and the optical properties for both the p- and the n-contact.

D8.3 summarises the efforts of optimising the IBC SHJ solar cell’s rear design using mainly numerical 2D simulations. Results from other work packages (WP5, capabilities of the patterning schemes; WP4, contact resistivities of the partners’ different layer stacks) were taken into consideration.

Deliverable Number	Deliverable name	Lead partner	Type	Dissemination level	Due date
D8.3	Report on the rear design of high efficiency IBC-SHJ solar cells	HZB			M24

## 2 Reducing Resistive Losses by Optimising the Contact Geometry (HZB)

This section discusses the optimisation of the contact geometry, e.g. the area ratio of the p- and the n-contact (alternately emitter and BSF contact) as well as the total pitch, using both a simple analytical model as well as advanced numerical 2D simulations (Sentaurus TCAD). Input parameters (range of pitch values, contact resistivities) were chosen in accordance with the findings presented in the work packages 4 and 5.

### 2.1 Geometrical Implications of the Contact Resistivities

The series resistance contribution related to the contact resistivities,  $R_{S,CR}$ , can be expressed as follows:

$$R_{S,CR} = \frac{\rho_p}{A_p} + \frac{\rho_n}{A_n}$$

Here  $\rho_p$  and  $\rho_n$  represent the contact resistivity of the p- and the n-contact, and  $A_p$  and  $A_n$  the contact area fractions. By assuming  $A_n = 1 - A_p$  and given set values for  $\rho_p$  and  $\rho_n$ ,  $R_{S,CR}$  becomes minimal if the following applies:

$$A_{p,min} = \frac{\sqrt{\rho_p}}{\sqrt{\rho_p} + \sqrt{\rho_n}}$$

**Figure 1** visualises the dependency of  $A_{p,min}$  on the p-contact resistivity for three different n-contact resistivities. The latter reflect realistic values being in accordance with recent TLM measurements for samples from all project partners.

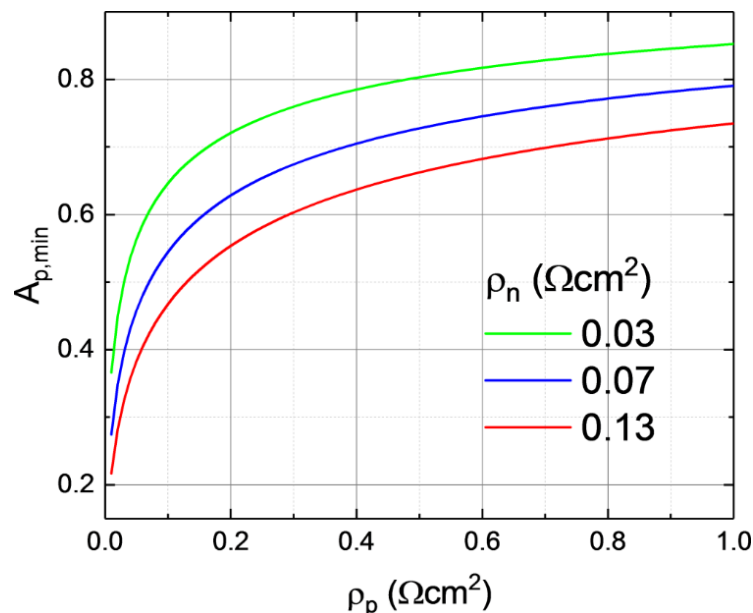


**Figure 1:** Emitter or p-contact area fraction yielding the minimum contact resistance over the corresponding p-contact resistivity for three different n-contact resistivities.

The calculation shows that even for very large discrepancies between the p- and n-contact, extreme shares of the p-contact area, i.e. a very much larger p- than n-contact area, tend to be unfavourable.

### Impact of the Bulk Resistance

The calculation in the previous section does not account for the impact of the bulk resistance on the resistive losses in the solar cell. A better approximation for the total series resistance can be achieved by adding a third summand, which is modelled using the following expression, proposed in [1]:

$$R_{S,Bulk} = \frac{d_{Em}(d_{Em} + d_{BSF})}{3t_W} \frac{\rho_B N_D}{(N_D + \Delta p)}$$

Here,  $d_{Em}$  represents half the width of the p-contact,  $d_{BSF}$  half the width of the n-contact and  $t_W$  the thickness of the wafer,  $N_D$  the dopant concentration,  $\Delta p$  the average excess minority carrier density at MPP conditions ( $10^{15} \text{ cm}^{-3}$ ) and  $\rho_B$  the wafer's bulk resistivity ( $3 \text{ } \Omega\text{cm}$ ). This bulk related term only accounts for the lateral current flow of majority carriers under the p-contact, thus its accuracy is limited. The total series resistance is then approximated to:

$$R_{S,total} \approx \frac{\rho_p}{A_p} + \frac{\rho_n}{A_n} + R_{S,Bulk}$$

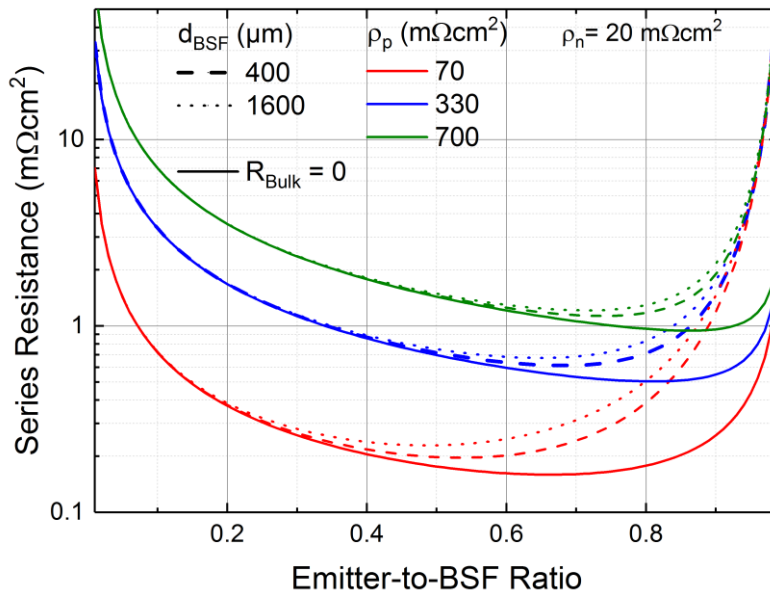


**Figure 2:** The series resistance vs. the metallised emitter-to-BSF ratio for multiple BSF widths ( $d_{BSF}$ ) and p-contact resistivities ( $\rho_p$ ); additionally the series resistance curve depending only on the contact resistivities is shown ( $R_{S,Bulk} = 0$ ).

**Figure 2** visualises the impact of the emitter-to-BSF ratio on the series resistance for different contact geometries (represented by fixed BSF width values) and varying p-contact resistivities. With  $R_{S,Bulk}$  set to 0, the optimum emitter-to-BSF ratio is equal to  $A_{p,min}$ , as shown in **Figure 1** (assuming identical contact resistivities for both the p- and the n-contact). By taking the bulk resistance into account, the overall series resistance increases and the optimum emitter-to-BSF ratio deviates from the ratio of the two contact resistivities (as expressed by the square-root relation of  $A_{p,min}$ ). The impact of the bulk resistance scales with the pitch. The increase of the latter is expressed by increasing constant BSF width values.

While the introduction of the bulk resistance has a very significant impact on the optimum emitter-to-BSF ratio, its influence on the total series resistance is less pronounced. Altering the contact resistivities, in particular the one of the p-contact, has a much more drastic effect

on both the optimum emitter-to-BSF ratio and on the total series resistance. Consequently, more effort should be put into decreasing the contact resistivities, especially the one of the p-contact, which usually exhibits much higher values than its n-contact counterpart (see TLM round robin).

The simulation study also illustrates that minimising the resistive losses in an IBC SHJ solar cell is a rather interconnected problem, as both the contact resistivities and the manufacturing procedure (setting the limits for the contact geometry) impact the resulting series resistance.

## 2.2 Validation with Sentaurus

The analytical model, presented in section 2.1, only accounts for resistive losses and describes these in a rather simplistic manner. A more accurate loss analysis can be performed by using numerical 2D simulations. **Figure 3** compares the optimum emitter-to-BSF ratios calculated either by the analytical model (minimum series resistance) or by Sentaurus TCAD (maximum fill factor) for various constant BSF widths. For each BSF width both approaches predict similar values, indicating the validity of the simple, analytical approach. Changes arise from the fact that Sentaurus also includes losses due to recombination, which become prevalent in particular for large BSF widths/pitch values, as for instance the collection efficiency of minority carriers decreases in the n-contact regions. Since the series resistance is usually the dominant loss parameter in IBC SHJ solar cells (as evidenced by the experimental results of various project partners), neglecting other loss contributions has only a minor effect on determining the optimum contact geometry.

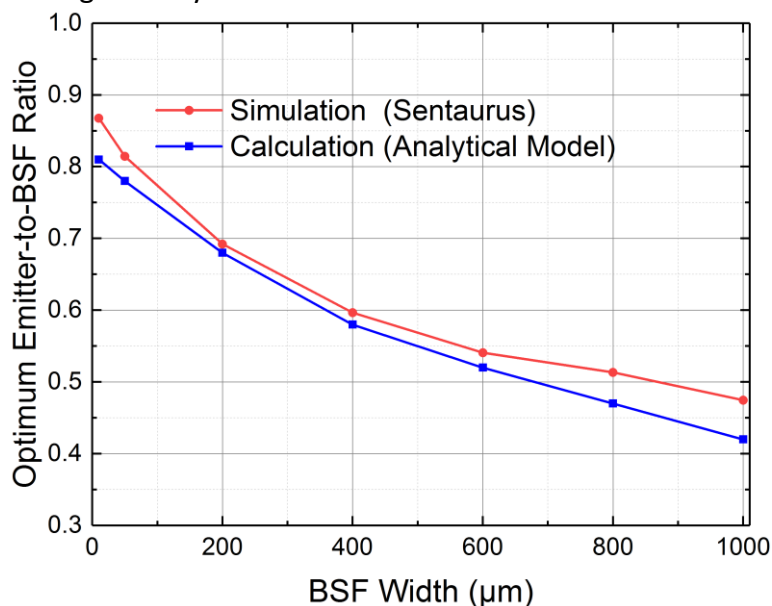


**Figure 3:** Optimum emitter-to-BSF ratios for different metallised BSF widths, with respect to either maximum FF values (Sentaurus simulation) or minimum series resistance values (analytical model).

## 2.3 Metallisation Gaps and Overlap

The calculations in the previous section did not account for regions where both the emitter and the BSF layer overlap and, more in general, for regions that are not metallised. Metallisation gaps are necessary to separate the two contacts, while a separation of the amorphous or nanocrystalline contact layers is not mandatory, as the lateral conductivity of these layers is usually low enough to prevent shunts. Hence, lateral current flow in non-

metallised emitter and BSF regions is expected to be negligible and the effective width of both the emitter and the BSF contact is determined by their metallisation coverage.

On the contrary, overlap regions are necessary in processes where the patterning of the emitter/BSF layers is based on multiple masking steps (see D5.1). The narrow overlap regions account for inherent inaccuracies of the subsequent masking steps.

In HZB’s photolithography design, the metallisation gap is formed by a 15  $\mu\text{m}$  overlap region and an equally wide non-metallised BSF region (30  $\mu\text{m}$  total metallisation gap). In reality, imperfect etching leads to a metallisation gap being slightly larger than 30  $\mu\text{m}$  and overlap regions being slightly narrower than 15  $\mu\text{m}$ . The same applies for HZB’s shadow mask process, with the dimensions of both the metallisation gap and the overlap region being considerably larger.

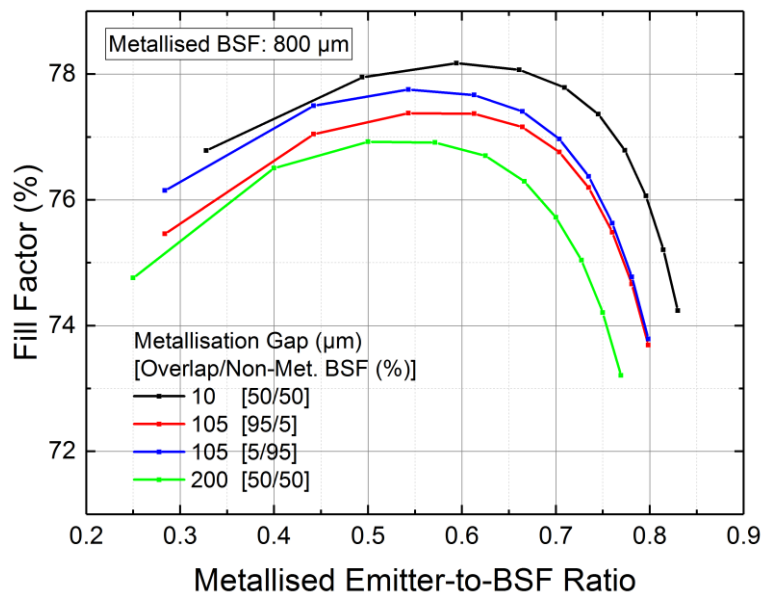


**Figure 4:** Dependency of the simulated fill factor on the metallised emitter-to-BSF ratio for different metallisation gap configurations.

**Figure 4** shows the dependence of the fill factor from the (metallised) emitter-to-BSF ratio for different metallisation gaps (with varying ratios of overlap/non-metallised BSF region). Ideally, the metallisation gap is as small as possible; however, constraints with respect to the manufacturing process can make larger gaps inevitable. Metallisation gaps with large overlap regions tend to deteriorate the FF more strongly than those with mainly non-metallised contact regions, as the former represent a parasitic p-i-n diode on top of the silicon wafer. Since the overlap area is not metallised, the corresponding diode is in open-circuit conditions (owing to the poor lateral conductivity of the amorphous and nanocrystalline silicon layers) and thus in blocking mode. Nevertheless, it represents an additional recombination path for minority charge carriers generated in its vicinity. The detrimental influence of the overlap region is particularly significant at lower emitter-to-BSF ratios, as in these cases the share of overlap area per total cell area is greater. Consequently, for larger metallised emitter ratios, the difference in device performance between gaps formed by an overlap or a non-metallised BSF region decreases.

## 2.4 Conclusion

A final example, illustrating the effects of gradually optimising the contact geometry, is given in Table 2. A simulated cell (Sentauros) with a BSF width of 400  $\mu\text{m}$  achieves a FF of 78.3 %. Decreasing the p-contact resistivity from 330 to 70  $\Omega\text{cm}^2$  increases the FF by 1.2 %abs. If then additionally the metallised emitter-to-BSF ratio is decreased (reducing the pitch from 2020 to 880  $\mu\text{m}$ ), the FF increases to 80.1 %, gaining another 0.6 %abs. With the pitch kept constant at a value of 2020  $\mu\text{m}$  (in this case the BSF width is increased to 904  $\mu\text{m}$ ), the FF still improves by 0.4 %abs, showing the importance of the emitter-to-BSF ratio.

**Table 2: Contact geometry optimisation and simulated fill factor trends**

Parameter Change	$m\text{-emr}^*$ (%)	$d_{\text{M,BSF}}^{**}$ ( $\mu\text{m}$ )	pitch ( $\mu\text{m}$ )	$\rho_p$ ( $\text{m}\Omega\text{cm}^2$ )	$\rho_n$ ( $\text{m}\Omega\text{cm}^2$ )	FF (%)
<b>initial</b>	79.2	400	2020	330	20	78.3
$\rho_p \downarrow$	79.2	400	2020	70	20	79.5
$\rho_p \downarrow, m\text{-emr} \downarrow, \text{pitch} \uparrow$	54.3	400	880	70	20	80.1
$\rho_p \downarrow, m\text{-emr} \downarrow, d_{\text{M,BSF}} \uparrow$	54.3	904	2020	70	20	79.9

\*  $m\text{-emr}$ : metallised emitter-to-BSF ratio

\*\*  $d_{\text{M,BSF}}$ : metallised BSF width

Minimising both the emitter and the BSF contact resistivity should be the primary focus in order to reduce resistive losses in an IBC SHJ solar cell. Depending on the magnitude and ratio of these two resistivities and the minimum feature size enabled by the patterning process, the total series resistance can be further decreased by optimising the emitter-to-BSF ratio.

### 3 Optimisation of the Contact Layer Stack (TUD)

As explained above, to reduce the contribution of each contact stack to device series resistance, an optimization of each layer and its interfaces is required. Moreover, reducing contact stack series resistance also entails field effect passivation which is linked to selectivity and transport mechanisms [2]. In this section, the optimization of SHJ contact stacks is discussed, based on TCAD Sentaurus numerical simulations.

#### 3.1 Contact Selectivity & Selective Transport

Contact selectivity is related to the asymmetry in carrier concentration at c-Si interface. Such a feature corresponds to the c-Si band bending ( $\Phi_{cSi}$ ) that allows c-Si Fermi level to be located close to the conduction band or valence band for n- or p-contact, respectively (see **Figure 5**) as result of contact build-in voltage ( $V_{bi}$ ). Indeed, maximizing  $V_{bi}$  enables maximum selectivity. Considering that thin film Si alloy's electron affinity is close to 4 eV, the selectivity is maximized by minimizing activation energy ( $E_a$ ), in case of n-contact and maximizing the difference: bandgap ( $E_g$ ) -  $E_a$  for the p-contact.

Selective transport is related to the collection of only electrons or holes through the n-contact or the p-contact stack. Thermionic emission and tunnelling mechanisms describe the transport of carriers through energy barriers and define the transport of carriers through energy discontinuities (energy barriers) formed at hetero-interfaces.

**Figure 5** depicts the energy barriers as patterned areas beneath conduction ( $q\psi_e(r)$ ) band or valence band ( $q\psi_h(r)$ ) from  $r = 0$  to  $r_{TCO}$  [2]. Accordingly, the selective transport concept is defined in terms of energy barriers at hetero-interfaces and also collecting free carrier density at the c-Si interface (contact selectivity) [2]. In SHJ selective contacts, hetero-interfaces are typically described by the c-Si/i-a-Si:H interface and the doped layer/TCO interface. Both band offsets at the hetero-interfaces, together with the band bending owing to the doped layers, build the aforementioned energy barriers. The band bending in doped layers is built by inherent space charge region inside the deposited material and it depends on  $E_a$ , and the TCO's work function ( $WF_{TCO}$ ), while the band offset is assumed constant in the SHJ concept that typically uses i-a-Si:H layer at c-Si interface and a TCO. It is worth noting that transport through the n-contact doped layer and the TCO is defined by direct tunnelling, while through the p-contact doped layer and TCO it is band to band tunnelling, since the TCO behaves as n-type degenerate semiconductor [3].

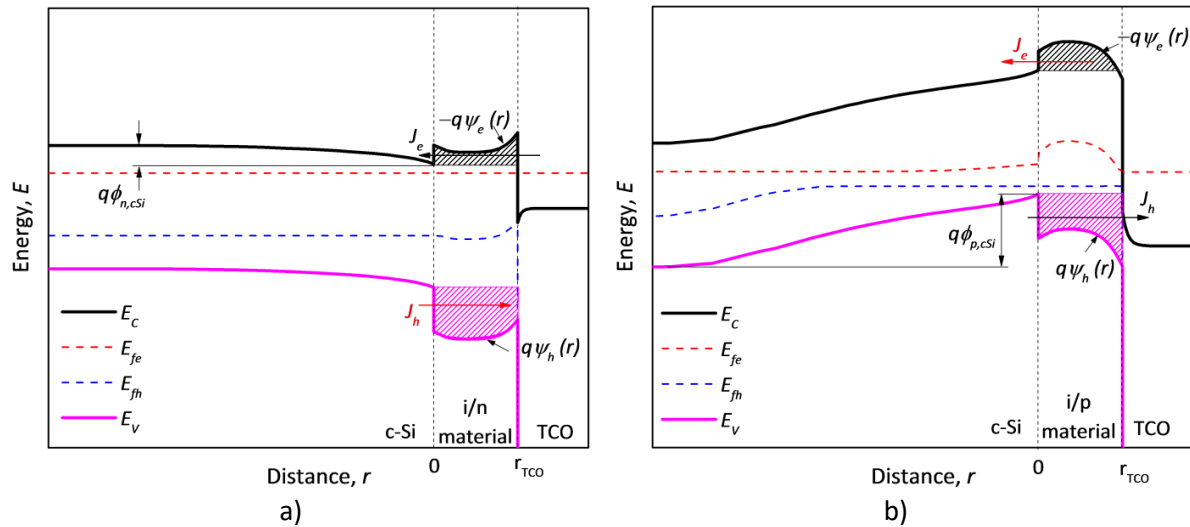


**Figure 5:** Band diagram of SHJ n-type (a) and p-type (b) contact. Patterned areas illustrate energy barriers for electrons in conduction band (magenta) and for holes in the valence band (black) [2].

The optimization of the contact stacks consists of concurrently i) maximizing the c-Si band bending ii) minimizing the energy barrier for collecting carriers and iii) maximizing the energy barrier for non-collecting carriers. To do so,  $E_a$  and  $E_g$  can be calibrated depending on the thin film Si alloy phase (amorphous and nanocrystalline) and alloy elements (oxygen, carbon), but also on  $WF_{TCO}$ , depending on the TCO material and its fabrication process.

It is worth noting that hetero-interfaces require special processing to keep the layer properties at the interface. For c-Si, a thin i-a-Si:H layer provides a good passivation and simultaneously works as buffer layer to keep the c-Si interface's integrity in terms of density of states/defects and band structure properties. A similar effect is expected in case of the doped layer/TCO hetero-interface, to avoid the formation of dipoles between these two adjacent interfaces.

### 3.2 Activation energy of doped layers

In this section, based on TCAD Sentaurus simulations, the effect of  $E_a$  on the transport of carriers is evaluated in terms of FF. More detailed information about the simulation parameters are described in [2]. As discussed in Section 3.1, both contact selectivity and selective transport depend on  $E_a$ . In general, lowering  $E_a$  increases  $V_{bi}$ , and also improves the band bending inside the doped layers as a result of the space charge region, owing to the properties of the materials surrounding both hetero-interfaces (c-Si and TCO). Accordingly, the FF evaluation is extended for different TCO work functions, as **Figure 6** reports.

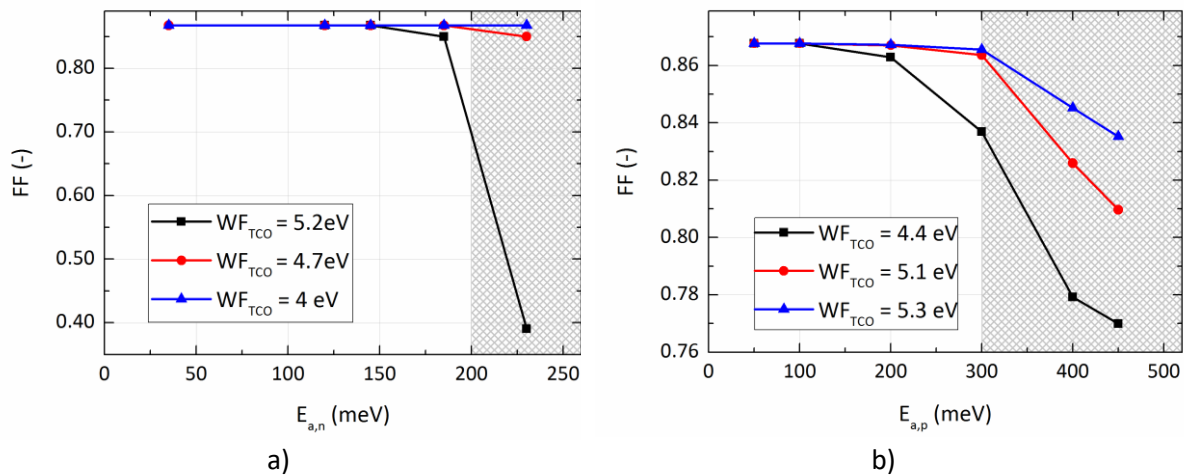


**Figure 6:** Simulated FF as a function of  $E_a$  at n-type (a) and p-type contact (b) for 7-nm thick doped layers and with respect to different  $WF_{TCO}$ . Patterned regions correspond to typical  $E_a$  of  $\alpha$ -Si:H doped for n- and p-contact [2].

The simulation in **Figure 6** shows that a clear decrease on FF is observed when the  $E_a$  increases for both n- and p-type contacts. This effect affects strongly the p-n junction, then the n+/n contacts (compare **Figure 6** (b) to (a)). Increasing  $E_a$ , the c-Si band bending is reduced and therefore the contact selectivity decreases. Concurrently, high  $E_a$  values increase the energy barrier of carriers to be collected and at the same time decrease the energy barrier of carriers not to be collected. Furthermore, the negative effect of relatively high  $E_a$  is mitigated depending on  $WF_{TCO}$  values, which modify the energy barrier size, thus explaining the different dependence of FF on  $E_a$  in case of low (high)  $WF_{TCO}$  values for the p-type (n-type) contact. Nevertheless, in general, low  $E_a$  values lead to high FF.

### 3.3 TCO work-function

**Figure 7** shows the FF as a function of  $WF_{TCO}$  for different  $E_a$ . For the p-type contact, an increase in FF is observed by increasing  $WF_{TCO}$ . On the contrary, in case of the n-type contact, the FF degrades for  $WF_{TCO}$  values higher than 4.7 eV. Interestingly, for both contact stacks, the FF becomes insensitive to  $WF_{TCO}$  for  $E_a$  values lower than 100 meV. As discussed above, lower  $E_a$  (i.e. higher doping) hinders the effect of induced band bending in doped layers. Simulation results demonstrate that two conditions could be implemented to improve the FF: (i) high  $E_a$  and a  $WF_{TCO}$  larger than 5.1 eV (smaller than 4.7 eV) for the p-type (n-type) contact, respectively; or (ii)  $E_a$  lower than 100 meV independently of the  $WF_{TCO}$ . Thus, the option (i) is limited by the TCO material and its processing parameters. Moreover, additional complexity comes from the fact that increasing  $WF_{TCO}$ , the conductivity of the TCO commonly decreases and vice-versa. On the other hand, the option (ii) allows the use of more types of TCO materials since only maximizing free states at TCO/doped layer interface matters in terms of higher conductivity. It is worth noting that depending on  $E_a$  and the doped layer's thickness,  $WF_{TCO}$  eventually influences on c-Si band bending. To avoid this effect, the thickness of doped layer has to be larger than the sum of the depletion region thicknesses from both interfaces, inside the deposited layers.

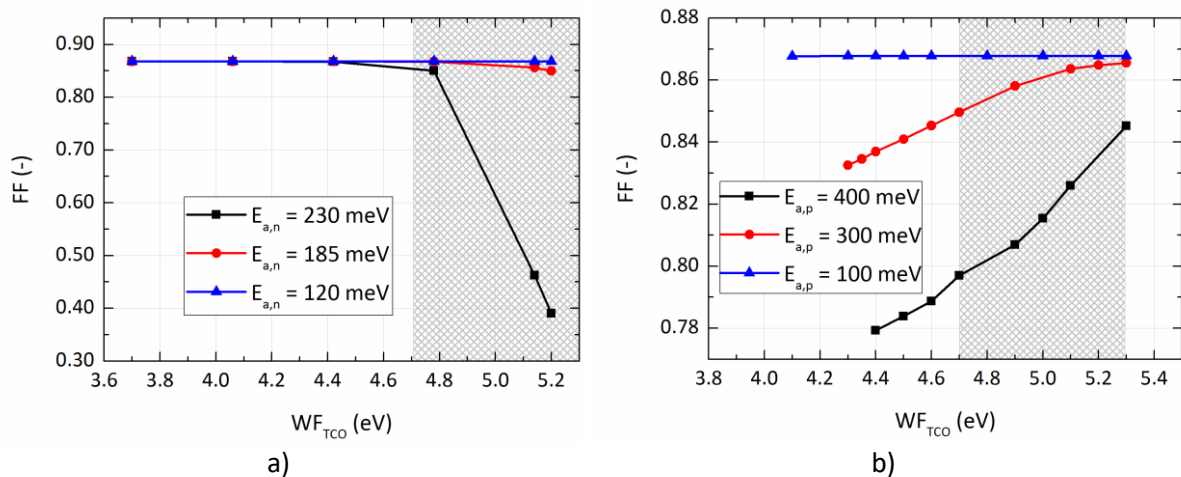


**Figure 7:** Simulated FF as a function of WF<sub>TCO</sub> at n-type (a) and p-type contact (b) for 7-nm thick doped layers and with respect to different E<sub>a</sub>. Patterned regions correspond to work function values of ITO 90 wt% In<sub>2</sub>O<sub>3</sub> and 10wt% SnO<sub>2</sub> [2].

Looking into the selective transport concept reported in [2], simulation results revealed that for the n-contact, lower E<sub>a</sub> values improve the barrier for non-collected carriers, and reduce the energy barrier size. A similar effect is reported for low WF<sub>TCO</sub> values. However, this effect is only apparent due to the reduction of non-collected carriers rather than the increase of collected carriers. This outcome is ascribed to the inherent fact that the conduction band offset is smaller than the valence band allowing an efficient collection of electrons.

In case of the p-contact, a low E<sub>a</sub> improves the hole collection more rather than reducing non-collected carriers. Similarly, WF<sub>TCO</sub> does not influence collected carriers, but it potentially reduces non collected carriers.

In thin film Si technology, low E<sub>a</sub> values correspond to highly doped amorphous structures, but E<sub>a</sub> is limited to values higher than 200 meV. To further reduce E<sub>a</sub>, a doped nanocrystalline silicon matrix can be used.

### 3.4 Band gap of p-type contact

As discussed in Section 3.1, the band bending at the c-Si interface depends on the E<sub>g</sub> of the deposited doped material. Maximum FF values are achieved for E<sub>g</sub>-E<sub>a</sub> difference, with E<sub>g</sub> = 1.7 eV and E<sub>a</sub> = 30 meV, resulting in 0.84 eV c-Si band bending. If E<sub>g</sub> increases to 2.1 eV, similar c-Si band bending is achieved, but for a relaxed 300 meV as E<sub>a</sub>. Indeed, such a values improve c-Si band bending but the structure becomes more sensitive to the TCO interface, since the work function mismatch potentially increases. To avoid this effect and fully take advantage of the improved c-Si band bending, one can combine wide band gap material layers (i.e. amorphous) followed by low bandgap nanocrystalline Si layers (low E<sub>a</sub>). Interestingly, such a structure mimics the growth of nanocrystalline structures that require an amorphous incubation layer. To evaluate the effect of a wide E<sub>g</sub> incubation layer by numerical simulations, two different structures are assumed: one with constant E<sub>g</sub> in the p-contact (including incubation layer) and the other using a wide E<sub>g</sub> for the incubation layer. The results are reported in **Table 3**. The use of a wide bandgap doped p-type layer as an incubation layer potentially boosts both FF and V<sub>OC</sub>. Simulated structures are insensitive to WF<sub>TCO</sub>, because

doped layers feature 50 meV as  $E_a$  at the doped layer/TCO interface in a similar way than in **Figure 7**.

**Table 3:** Summary of external parameters of IBC-SHJ solar cells featuring different p-type doped incubation layers. The p-type doped layer in contact with the TCO is p-type nc-Si:H ( $E_g = 50$  meV). [2]

Incubation layer	$J_{sc}$ (mA/cm <sup>2</sup> )	$V_{oc}$ (mV)	FF (%)	$\eta$ (%)
<b>p-type a-Si:H</b>	41.4	744	84.9	26.2
<b>p-type SiO<sub>x</sub> or p-type SiC<sub>x</sub></b>	41.5	754	86.8	27.2

### 3.5 Summary

In order to provide guidelines for improving contact stack quality in terms of FF, the main parameters of deposited layers have been analysed. In general, low values of  $E_a$  in doped layers are required to improve FF. Additionally, the contact stack needs to be optimized depending on contact type and  $E_a$  values, TCO work function and bandgap condition transport. According to simulation results, the following conditions lead to an optimized contact stack:

1. For n-contact, doped layer with low  $E_a$  combined with any TCO, or relatively high  $E_a$  combined with a TCO featuring low  $WF_{TCO}$ .
2. For p-contact, a combination of wide  $E_g$  as incubation layer in combination with low  $E_a$  layer that reduce contact resistance with any TCO. As an alternative, a relatively high  $E_a$  combined with a high work function TCO also improves the collection of holes at the p-contact.

## 4 Risks and Interconnections

### 4.1 Risks/problems encountered

Neither risks nor significant problems were encountered in carrying out the work for this deliverable.

### 4.2 Interconnections with other deliverables

The simulation results provided in this report lay out design guidelines helping to achieve the goals set in D4.1, D4.2 and D5.3 (devices with high  $V_{OC}$  and  $FF$ , as well as an efficiency greater than 26 %). As discussed above, the simulations show clearly that many parameters need to be considered in optimizing the interdigitated contact structure (minimising the resistive losses) in an IBC SHJ solar cell: Both the contact resistivities and the manufacturing procedure (setting the limits for the contact geometry) impact the resulting series resistance. Thus, further interconnections exist with the contact-related deliverable D4.4 (plating), D5.1 (patterning schemes), D6.1 (tool specs for in-situ masking) and, ultimately, to D8.5 (pathway to highest efficiencies).

## 5 Conclusion

We have used analytical calculations and numerical simulations to optimise the contact geometry of IBC-SHJ solar cells. Using the analytical calculations presented in the beginning, it becomes clear, more effort should be put into decreasing the contact resistivities, especially the one of the p-contact, which usually exhibits much higher values than its n-contact counterpart.

Key to optimising the contact layer stack and thus reducing the contact resistivity is using doped layers with low activation energies, or TCO materials with an appropriate work function. For the n-contact, doped layers with low activation energies will work with any TCO material; for n-contact layers with higher activation energies, the TCO's work function should be as low as possible.

For the p-contact, a wide band gap material as an incubation layer in combination with a p-type layer with a low activation energy yields low contact resistivities even for TCO materials with a low work function. In case of a p-contact layer with a higher activation energy, a TCO material with a high work function is necessary to enable efficient current extraction.

## 6 References

- [1] P. J. Verlinden *et al.*, “Simple power-loss analysis method for high-efficiency Interdigitated Back Contact (IBC) silicon solar cells,” *Sol. En. Mat. Sol. Cells*, vol. 106, p. 37 - 41, 2012.
- [2] P. Procel, G. Yang, O. Isabella, and M. Zeman, “Theoretical Evaluation of Contact Stack for High Efficiency IBC-SHJ Solar Cells,” *Sol. En. Mat. Sol. Cells*, vol. 186, p. 66 - 77, 2018.
- [3] A. Klein *et al.*, “Transparent conducting oxides for photovoltaics: Manipulation of fermi level, work function and energy band alignment,” *Materials (Basel)*., vol. 3, no. 11, pp. 4892–4914, 2010.